

Anisotropic Dzyaloshinskii-Moriya Interaction in ultra-thin epitaxial Au/Co/W(110)

Lorenzo Camosi,^{1,2,*} Stanislas Rohart,³ Olivier Fruchart,^{1,4,5,2} Stefania Pizzini,^{1,2}

Mohamed Belmeguenai,⁶ Yves Roussigné,⁶ Andreï Stachkevitch,^{6,7} Salim

Mourad Chérif,⁶ Laurent Ranno,^{1,2} Maurizio de Santis,^{1,2} and Jan Vogel^{1,2,†}

¹Univ. Grenoble Alpes, F-38000 Grenoble, France

²CNRS, Institut Néel, F-38000 Grenoble, France

³Laboratoire de Physique des Solides, Université Paris-Sud,

CNRS UMR 8502, F-91405 Orsay Cedex, France

⁴CNRS, SPINTEC, F-38000 Grenoble, France

⁵CEA, INAC-SPINTEC, F-38000 Grenoble, France

⁶LSPM-CNRS, Université Paris XIII-Sorbonne Paris Cité, F-93430 Villetaneuse, France

⁷International laboratory “MultiferrLab”, ITMO University, St. Petersburg, Russia

We have used Brillouin Light Scattering spectroscopy to independently determine the in-plane Magneto-Crystalline Anisotropy and the Dzyaloshinskii-Moriya Interaction (DMI) in out-of-plane magnetized Au/Co/W(110). We found that the DMI strength is 2.5 larger along the $bcc[001]$ than along the $bcc[\bar{1}10]$ direction. We use analytical considerations to illustrate the relationship between the crystal symmetry of the stack and the anisotropy of microscopic DMI. This shows that systems with two-fold symmetry are promising for realizing isolated elliptical skyrmions or anti-skyrmions.

An anti-symmetric exchange interaction, the Dzyaloshinskii-Moriya Interaction (DMI), was first theoretically predicted by Dzyaloshinskii using symmetry arguments in bulk magnetic systems [1]. Then Moriya [2] demonstrated the anti-symmetric spin coupling in systems with a lack of inversion symmetry, by including spin-orbit coupling in the super-exchange interaction. Fert and Levy [3] pointed out that high spin-orbit scattering centers can break the indirect exchange symmetry. The study of DMI presents a particular interest since it can stabilize chiral magnetic textures like skyrmions. Skyrmions are magnetic solitons characterized by chiral vortex-like spin configurations. They belong to a different topological space than the ferromagnetic one, so that hopes for a robust topological protection have been raised.

Ground-state triangular skyrmion-lattice phases were the first to be found experimentally in 2009 [4], in a magnetic compound with lack of bulk inversion symmetry. In 2013, isolated circular skyrmions were observed as metastable objects in ultra-thin magnetic films, the breaking of symmetry arising from the interfaces. However, a strong magnetic field, ultra-high vacuum and low temperatures were required [5]. Later, isolated skyrmions were stabilized at room temperature in capped films [6, 7], opening the route to patterning circuits for their manipulation, with the recent achievement of their motion by spin orbit torques [8, 9]. It has been demonstrated recently that skyrmions can display a non-cylindrical symmetry in anisotropic environments. The effect of spatially modulated exchange energy and magnetocrystalline anisotropy on the skyrmion shape has been theoretically analyzed [10] and experimentally investigated [11] in ultra-thin films, while a distorted skyrmion lattice [12] has been evidenced in a bulk system due to an anisotropic DMI arising in a mechanically-

strained single-crystal.

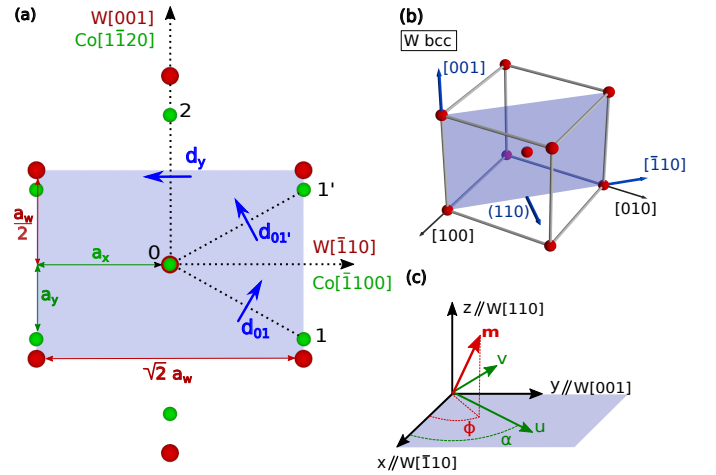


Figure 1: (a) Superposition of the W(110) and the strained Co (0001) surfaces with the Nishiyama-Wassermann relationship (b) Tungsten bcc unit cell with the (110) surface highlighted (c) Illustration of the geometry and notation used to describe the magnetization ($\theta; \phi$) and the directions (α) in the $bcc(110)$ crystal framework

In this paper, we investigate epitaxial Au/Co/W(110), a thin-film system that displays a large two-fold anisotropic DMI, which we measured directly by Brillouin Light Scattering spectroscopy (BLS). The evidence of anisotropic DMI in ultra-thin stacks opens the possibility for stabilizing isolated non-circular skyrmions or even anti-skyrmions, topological objects which until now have been predicted only theoretically [13, 14].

The sample stack is grown by pulsed laser deposition, and crystallographic properties are investigated in-situ.

The (11 $\bar{2}$ 0) surface of a commercial Al₂O₃ single crystal is used as the substrate for growing at room temperature a thin film of Mo (0.8 nm) followed by the deposition of a 8 nm thick W film. The stack is then annealed at 1200 K for 1 h. During this annealing the Mo underlayer promotes the selection of a unique epitaxial relationship, avoiding twins and yielding a single-crystalline film [15]. Reflection High-Energy Electron Diffraction (RHEED)[16] confirms the disappearance of the W twins and the correct epitaxial relationship (Fig. 1).

Ultrathin Co films are then deposited, either as a wedge in order to study the thickness-dependent properties [16] and confirm the layer-by-layer deposition by Scanning Tunneling Microscopy [16], or with a uniform thickness ($t = 0.65$ nm) for the BLS measurements.

The best condition for layer-by-layer growth was obtained by progressively warming the sample from room temperature to 448 K while the Co thickness increases from 0 to 1.5 nm. The immiscibility between Co and W guarantees a flat and sharp interface. RHEED and Grazing incidence X-ray diffraction (GIXRD) patterns demonstrate the retained single crystal feature through the so-called Nishiyama-Wassermann epitaxial relationship [16]. The lattice misfits along the main in-plane crystallographic directions are $\Delta a_{bcc[\bar{1}10]} = \frac{\sqrt{2}a_W - \sqrt{3}a_{Co}}{\sqrt{2}a_W} = 2.98\%$ and $\Delta a_{bcc[001]} = \frac{a_W - a_{Co}}{a_W} = 20.79\%$ where a_W and a_{Co} are respectively the bulk *bcc* and *hcp* lattice parameters. Along the *bcc*[\bar{1}10] direction the Co is expected to grow pseudomorphically ($a_x = \sqrt{2}/2a_W$, with a_x defined in Fig.1), up to 10 Co monolayers (1ML $\simeq 0.2$ nm) [17]. Along the *bcc*[001] direction, the misfit instead is large implying that the Co structure relaxes for a thickness between 2 and 4 ML ($a_y = 3.56/4.56 \frac{a_W}{2}$ [17]), where a_y is defined in Fig.1. Along this direction, the Co-W crystal forms a superstructure with a period of $14a_y$ (1.5 nm). This is reasonably smaller than the characteristic magnetic length scales even in ultrathin Co films, so that from the micromagnetic point of view the system can be considered uniform with averaged quantities and with a C2 symmetry.

Finally, a 2 nm-thick *fcc* Au(111) cap layer (C6 crystal symmetry) is deposited in order to promote out-of-plane anisotropy and protect the stack from oxidation. GIXRD measurements show that the Co/W interface is hardly modified by the capping layer [16] and the stressed Co

layer does not significantly changes its C3 crystal symmetry. Hence we expect the contribution of the Au/Co interface to the anisotropic properties to be negligibly small.

The Brillouin Light Scattering spectroscopy was performed in the Damon-Eshbach (DE) configuration [18]. This technique is particularly suited for the study of anisotropic systems because it allows to extract the magnetic properties independently along any direction. An external magnetic field H_{ext} saturates the magnetization along an in-plane direction. A photon beam, generated by a laser ($\lambda = 532$ nm), strikes the sample in the plane perpendicular to the magnetic field with an incidence angle $0^\circ < \theta_{\text{inc}} < 60^\circ$ in order to vary the spin wave (SW) wave vector involved in the scattering process $k_{\text{SW}} = 4\pi \sin(\theta)/\lambda$. We call α the angle between \mathbf{k}_{SW} (the direction along which the magnetization varies) and the *bcc* [\bar{1}10] crystallographic direction (Fig.1). A 2x3 pass Fabry-Perot interferometer allows to analyze the back-scattered light and to study the Stokes (S) and anti-Stokes (AS) spectrum generated by the scattering process between the laser photons and the SWs for different α values. The BLS spectrum in systems with DMI can be separated in a symmetric $f_0 = (|f_S| + |f_{AS}|)/2$ and an antisymmetric component $f_{\text{anti}} = (|f_S| - |f_{AS}|)/2$. The study of f_0 with H_{ext} along the main crystallographic directions allows to estimate the magneto-crystalline anisotropy (MCA) constants K_i in the direction of the applied field, while f_{anti} allows to extract the DMI sign and strength acting on a Néel spin cycloid along the SW wavevector.

The twofold supercrystal symmetry induces a biaxial MCA energy density that can be formulated in the second order approximation including the out-of-plane shape anisotropy ($K_d = \frac{1}{2}\mu_0 M_s^2$):

$$E_{\text{anisotropy}} = -(K_{\text{out}} - K_d) \cos^2 \theta - K_{\text{in}} \sin^2 \theta \cos^2 \phi \quad (1)$$

where θ and ϕ describe the magnetization direction (Fig.1) and K_{out} and K_{in} are respectively the out-of-plane and the in-plane easy axis MCA constants. The symmetric frequencies $f_0^{[\bar{1}10]}$ and $f_0^{[001]}$, when H_{ext} is respectively applied along [\bar{1}10] and [001], can be calculated [19] as,

$$f_0^{[001]} = \frac{\gamma\mu_0}{2\pi} \sqrt{[H_{\text{ext}}^{[001]} - H_{\text{in}} + Jk_{\text{SW}}^2 + P(k_{\text{SW}}t)M_s][H_{\text{ext}}^{[001]} - H_{\text{out}} + Jk_{\text{SW}}^2 - P(k_{\text{SW}}t)M_s]} \quad (2)$$

$$f_0^{[\bar{1}10]} = \frac{\gamma\mu_0}{2\pi} \sqrt{[H_{\text{ext}}^{[\bar{1}10]} + H_{\text{in}} + Jk_{\text{SW}}^2 + P(k_{\text{SW}}t)M_s][H_{\text{ext}}^{[\bar{1}10]} - H_{\text{out}} + H_{\text{in}} + Jk_{\text{SW}}^2 - P(k_{\text{SW}}t)M_s]} \quad (3)$$

where γ is the gyromagnetic ratio, $J = \frac{2A}{\mu_0 M_s}$ is the SW

stiffness with A the exchange stiffness and M_s the spon-

taneous magnetization, $P(k_{\text{SW}}t) = 1 - \frac{1 - \exp(-|k_{\text{SW}}|t)}{|k_{\text{SW}}|t}$ is a geometric factor associated to the SW dynamics with t the sample thickness, H_{out} and H_{in} are the anisotropy fields. By analyzing the spectra in Fig. 2 one can have a numerical estimation of the MCA constants. In this work, the S-AS peaks occur for small values of k_{SW} , i.e. $Jk_{\text{SW}}^2 \ll H_{\text{ext}}$, so that it is possible to neglect exchange contribution to the resonance BLS peaks. The spontaneous magnetization ($M_s = 1.15 \cdot 10^6$ A/m) is inferred from the out-of-plane hysteresis loop obtained with a vibrating sample magnetometer (VSM). Evaluating $f_0^{[001]} = 8.53$ GHz and $f_0^{[\bar{1}10]} = 15.24$ GHz with respectively $\mu_0 H_{\text{ext}}^{[\bar{1}10]} = 0.5$ T and $\mu_0 H_{\text{ext}}^{[001]} = 0.6$ T we obtain $K_{\text{in}} = \frac{1}{2}\mu_0 M_s H_{\text{in}} = 136$ kJ/m³ and $K_{\text{out}} - K_d = \frac{1}{2}\mu_0 M_s H_{\text{out}} = 199$ kJ/m³. Anomalous Hall Effect measurements performed on the same sample confirm the anisotropy values, validating the approach. Note that published results on the same system [20] showed a comparable out-of-plane anisotropy [16], but a larger in-plane anisotropy.

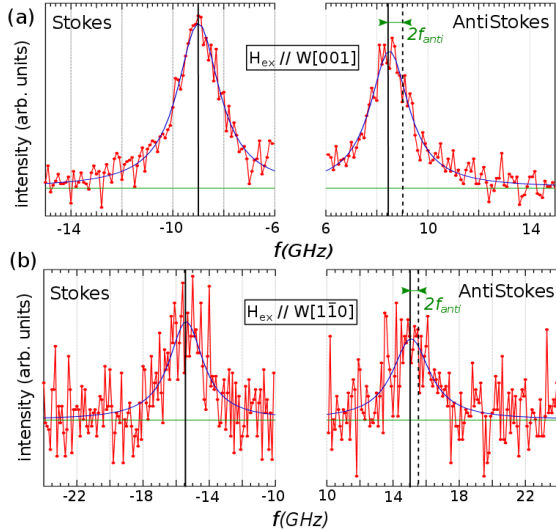


Figure 2: BLS spectra on Au/Co(0.65 nm)/W(110) with k_{SW} along the two in-plane symmetry axes. Red: experimental data. Blue line: data fit with Lorentzian functions. Green line: background fit. In the AS spectra, the distance between the continuous and dashed black lines shows the frequency shift between S and AS peaks. (a) BLS spectrum with $\mu_0 H_{\text{ext}} = 0.6$ T parallel to the $bcc[001]$ axis and $k_{\text{SW}} = 8.08/\mu\text{m}$ parallel to the $bcc[\bar{1}10]$ axis (b) BLS spectrum with $\mu_0 H_{\text{ext}} = 0.5$ T parallel to the $bcc[\bar{1}10]$ axis and $k_{\text{SW}} = 18.09/\mu\text{m}$ parallel to the $bcc[001]$ axis.

The difference $2f_{\text{anti}}$ arises from the different DMI effect on SW modes with opposite k_{SW} [21, 22]. In ultrathin films DMI is the only physical phenomenon liable to break the S-AS peak symmetry. BLS is thus particularly suitable for the investigation of anisotropic DMI, especially because the extracted data are independent from

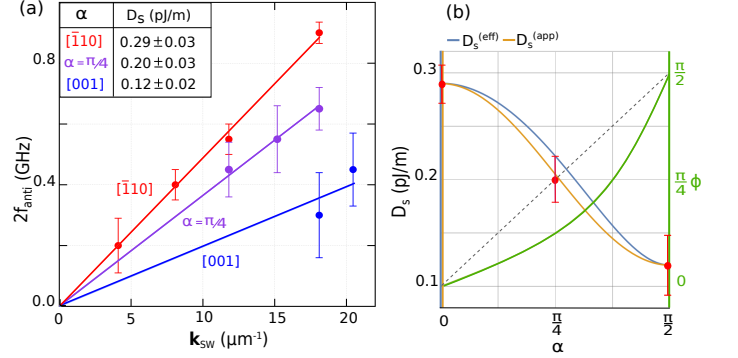


Figure 3: (a) S-AS frequency shift ($2f_{\text{anti}}$) as a function of SW wave-vector (k_{SW}) for different in-plane directions α . The dots are the experimental data and the lines are linear fit yielding the DMI strength (D_s). (b) Blue and orange lines: micromagnetic calculated $D_s^{(\text{eff})}$ (Eq.10) and $D_s^{(\text{app})}$ (Eq.8) as a function of the in-plane directions (ϕ); red dots: D strength evaluated from the experimental data; green line: micromagnetic calculated magnetization direction promoted by DMI (Eq.9) as a function of the crystallography directions; dashed line: Néel-like cycloid

any other anisotropy present in the system such as MCA, and from the strength of H_{ext} . The SW frequency shift in a system with interfacial DMI [$D(t) = D_s/t$] in the DE geometry can be formulated as [21, 23]:

$$2f_{\text{anti}} = \frac{2\gamma}{\pi} \frac{D(t)}{M_s} k_{\text{SW}} = \frac{2\gamma}{\pi} \frac{D_s}{M} k_{\text{SW}}. \quad (4)$$

M , the magnetic moment per unit surface ($M = M_s t$), can be obtained directly from VSM measurements, allowing a thickness-independent determination of the DMI strength, D_s . In Fig.(3) $2f_{\text{anti}}$ is plotted as a function of k_{SW} along the main axes ($bcc[001]$; $bcc[\bar{1}10]$) and along an intermediate direction ($\alpha = \pi/4$). The points in the plot are extracted from the center of the Lorentzian distribution used to fit the S and AS peaks (Fig.2). The error bars (δf) are obtained by a Levenberg-Marquardt error algorithm. The difference in the magnitude of errors (Fig.3) between the in-plane directions is related to an instrumental issue that leads to a decrease of the signal-to-noise ratio in the BLS spectra when the magnon frequency increases (Fig.2).

The plot in Fig.(3) demonstrates along all directions the occurrence of a clockwise chirality and strongly anisotropic DMI. In the table in Fig.(3)(a) the values of D_s parallel to the H_{ext} direction are shown. The DMI strength increases by a factor of 2.5 going from the $bcc[001]$ to the $bcc[\bar{1}10]$ direction passing an intermediate value when SWs propagate at $\alpha = \pi/4$.

In order to understand the relation between the crystal symmetry and the micromagnetic DMI anisotropy, we propose calculations starting from the atomic DMI

formulation (Eq.5). This consideration does not aim at the quantitative evaluation of DMI, but illustrates how atomic DMI vectors \mathbf{d}_{ij} between Co atoms i and j at various sites, add up or compensate to yield global micromagnetic D constants along the main symmetry axes ($bcc[\bar{1}10]$ and $bcc[001]$).

$$E_{DMI} = \sum_{ij} \mathbf{d}_{ij} \cdot (\mathbf{m}_i \times \mathbf{m}_j) \quad (5)$$

Following the Moriya symmetry rules, \mathbf{d}_{ij} is parallel to the normal of the triangle delimited by the magnetic atoms and the scattering center[3]. We consider the Co/W superstructure and we restrict the calculation to the Co first neighbors. The Co/W cell relation with highest symmetry is shown in Fig.(1). Indeed in the Co/W superlattice the position of the W atoms with respect to the Co atoms changes from one Co unit cell to the next. Thus we can expect \mathbf{d}_{ij} vectors with different strengths and directions. If the analyzed magnetic configurations have a characteristic length (l) much larger than the supercell parameter ($14a_x$) one can reduce the calculation to a single Co cell with $\langle \mathbf{d}_{ij} \rangle$ vectors as the average of all the \mathbf{d}_{ij} for the same bonds on the superlattice. Along the 02 bond the W atoms are aligned with the Co atoms and the $\langle \mathbf{d}_{ij} \rangle$ will lie in the crystal plane. The bonds 01' and 01 are symmetric with respect to the W atoms and they have the same length $|\mathbf{r}_{01}| = |\mathbf{r}_{01'}|$. Then we can expect that the in-plane components will average to zero and consider that the vectors have the same modulus ($\langle d \rangle = \langle d_{01'} \rangle = \langle d_{01} \rangle$). Moreover the previous condition ($l \gg 14a_x$) allows describing the magnetization in a continuous medium approach and expressing \mathbf{m}_j as the Taylor expansion centered in i . Then developing the calculations [16] and using the notation of the Lifshitz invariants $L_{jk}^{(i)} = m_j \frac{\partial m_k}{\partial i} - m_k \frac{\partial m_j}{\partial i}$ the DM energy can be written:

$$E_{DM} = - \int \left[D_s^{(x)}(D_s, \beta) L_{xz}^{(x)} + D_s^{(y)}(D_s, \beta) L_{yz}^{(y)} \right] d^2 r \quad (6)$$

the equation presents a two-fold symmetry with two DMI constants $D_s^{(x)} = D_s \cot \beta$ and $D_s^{(y)} = D_s \frac{\sin \beta + \langle d_y \rangle / \langle d \rangle}{\cos \beta}$ that depend on three parameters $D_s = \frac{\langle d \rangle}{a}$, $\beta = \arctan(a_y/a_x)$ and $\langle d_y \rangle / \langle d \rangle$. The experimental data for $\alpha = 0$ and $\alpha = \pi/2$ in Fig. (3) allow to evaluate the DMI constants. Setting $\beta = 0.51$ inferred from GIXRD [16] we obtain $D_s = 0.186 \text{ pJ/m}$ and $\langle d_y \rangle / \langle d \rangle = 0.14$. The value of D_s is in agreement with the one found for sputtered systems[24], however the complex superstructure does not allow a quantitative explication for the difference between $\langle d \rangle$ and $\langle d_y \rangle$.

It is possible to generalize the discussion to every ultrathin magnetic system with interfacial DMI and a twofold symmetry. Considering a new basis $(\hat{u}, \hat{v}, \hat{z})$ (see Fig.(1), turned at an angle $\alpha = (\hat{x}, \hat{u})$ with respect to the initial

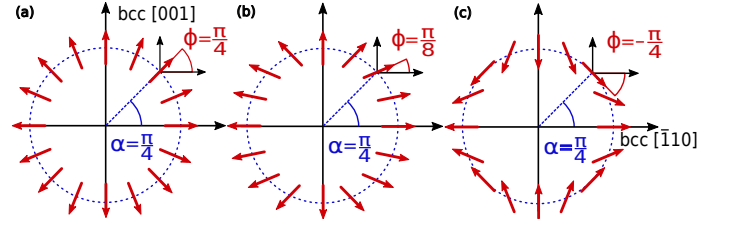


Figure 4: Polar plot of magnetization direction (ϕ) promoted by DMI as a function of the in plane direction of variation α (Eq. 9) for different $(D_s^{(x)}; D_s^{(y)})$ values: (a) $D_s^{(x)} = D_s^{(y)}$ (b) $D_s^{(x)} = 2.5 D_s^{(y)}$ (c) $D_s^{(x)} = -D_s^{(y)}$

basis, the DMI energy of a uni-dimensional spin modulation propagating along \hat{u} reads:

$$E_{DM}(\alpha) = - \int \left[\cos^2(\alpha) D_s^{(x)} + \sin^2(\alpha) D_s^{(y)} \right] L_{uz}^{(u)} d^2 r - \int \left(D_s^{(x)} - D_s^{(y)} \right) \cos(\alpha) \sin(\alpha) L_{uz}^{(v)} d^2 r. \quad (7)$$

It presents two different types of Lifshitz invariants that describe a DMI stabilizing different spin configurations in competition [25]. The first term $L_{uz}^{(u)}$ describes the well known result of an interfacial DMI promoting a Néel cycloid. The second term $L_{uz}^{(v)}$ evidences that the interfacial DMI in a two-fold symmetry system can stabilize a Bloch spiral. This last component vanishes along the main axes and has maxima proportional to the difference of the DMI constants $(D_s^{(x)} - D_s^{(y)})$ when $\alpha = \pi/4 + n\pi/2$. It means that in a general two-fold system the DMI promotes Néel cycloids along the main axes and a mixed configuration between a Néel cycloid and a Bloch spiral along the intermediate directions.

In order to understand the BLS data at $\alpha = \pi/4$, we evaluate the DMI energy for a SW described as $\mathbf{m}(u) = \mathbf{M} + \delta \mathbf{m}(u)$, with $\mathbf{M} \propto \hat{v}$ (parallel to \mathbf{H}_{ext} , due to the DE geometry) and $\delta \mathbf{m}(u)$ lying in the (\hat{u}, \hat{z}) plane. The apparent DMI constant $D_s^{(app)}$ is estimated from the DMI energy density of the SW [16]. As a function of α , we find

$$D_s^{(app)} = D_s^{(x)} \cos^2 \alpha + D_s^{(y)} \sin^2 \alpha \quad (8)$$

The plot of Eq.8 in Fig.(3)(b) shows a very good agreement with the experimental data.

In a more general case, the rotation plane of a spin spiral is free in order to minimize the energy. Writing ϕ as the angle of such a plane with respect to the \hat{x} axis (Fig. (1)), we estimate the optimum relation between ϕ and α :

$$\tan \phi = \left(\frac{D_s^{(y)}}{D_s^{(x)}} \right) \tan \alpha \quad (9)$$

with an effective DMI constant which represents the maximum DMI energy gain possible in the corresponding direction

$$D_s^{eff} = D_s^{(x)} \cos \alpha \cos \left[\arctan \left(\frac{D_s^{(y)}}{D_s^{(x)}} \tan \alpha \right) \right] + D_s^{(y)} \sin \alpha \sin \left[\arctan \left(\frac{D_s^{(y)}}{D_s^{(x)}} \tan \alpha \right) \right] \quad (10)$$

Hence setting $D_s^{(x)} = 2.5D_s^{(y)}$ it is possible to obtain the $D_s^{(eff)}(\alpha)$ and the $\phi(\alpha)$ for Au/Co/W(110) (Fig.3(b))(Fig.4(b)).

Studying Eqs.(9)(10) we can emphasize two interesting cases. First, setting isotropic conditions ($D_s^{(x)} = D_s^{(y)}$) we obtain the well-known result of a DMI stabilizing only Néel cycloids ($\alpha = \phi$) (Fig.4(a)). However, when $D_s^{(y)}$ and $D_s^{(x)}$ have opposite signs [26], Eqs. (9) and (10) show that anti-skyrmionic spin textures with $\phi \propto -\alpha$ are promoted (Fig.4(c)), i.e. cycloids with opposite chiralities along the main orthogonal axes, while chiral Bloch spirals are expected for intermediate angles. The variation $\phi(\alpha) \propto -\alpha$ implies that the winding number is $W = [\phi(\alpha)]_{\alpha=0}^{\alpha=2\pi} / 2\pi = -1$ [27], indeed the signature of an anti-skyrmion.

In conclusion, we investigated DMI in an out-of-plane magnetized epitaxial Au/Co(0.65 nm)/W(110) trilayer. The DMI in this system promotes a clockwise chirality with a DMI strength 2.5 times larger along $bcc[\bar{1}10]$ than along $bcc[001]$. This anisotropy arises from the two-fold symmetry of the Co/W(110) stack. We used a phenomenological model to highlight the link between the atomic DMI at the Co/W(110) interface based on its expected superlattice, with the resulting micromagnetic uniaxial DMI. Under such conditions, DMI gives rise not only to Néel cycloids, but to mixed cycloid/spiral textures [Fig.4(b)]. This experimental evidence of a strongly-anisotropic DMI is the first important step for the stabilization in a magnetic thin film of deformed isolated skyrmions and antiskyrmions.

We express our thanks Philippe David and Valerie Guisset for the crucial support in the sample growth. We acknowledge a grant from the Laboratoire d'excellence LANEF in Grenoble (ANR-10-LABX-51-01), and support from the ANR (project ANR-14-CE26-0012 ULTRASKY) and from the Government of the Russian Federation (Grant 074-U01). We acknowledge the European Synchrotron Radiation Facility and the french CRG-IF beamline for providing beam time.

[†] Electronic address: jan.vogel@neel.cnrs.fr

- [1] I. Dzyaloshinskii, Sov. Phys. JETP **5**, 1259 (1957).
- [2] T. Moriya, Phys. Rev. **120**, 91 (1960).
- [3] A. Fert and P. M. Levy, Phys. Rev. Lett. **44**, 1538 (1980).
- [4] S. Mühlbauer, B. Binz, F. Jonietz, C. Pfleiderer, A. Rosch, A. Neubauer, R. Georgii, and P. Böni, Science **323**, 915 (2009).
- [5] N. Romming, C. Hanneken, M. Menzel, J. E. Bickel, B. Wolter, K. von Bergmann, A. Kubetzka, and R. Wiesendanger, Science **341**, 636 (2013).
- [6] C. Moreau-Luchaire, C. Moutafis, N. Reyren, J. Sampaio, C. A. F. Vaz, N. Van Horne, K. Bouzehouane, K. Garcia, C. Deranlot, P. Warnicke, et al., Nat. Nanotechnol. **11**, 444 (2016).
- [7] O. Boulle, J. Vogel, H. Yang, S. Pizzini, D. d. S. Chaves, A. Locatelli, T. O. Montes, A. Sala, L. D. Buda-Prejbeanu, O. Klein, et al., Nat. Nanotechnol. **11**, 449 (2016).
- [8] W. Jiang, P. Upadhyaya, W. Zhang, G. Yu, M. B. Jungfleisch, F. Y. Fradin, J. E. Pearson, Y. Tserkovnyak, K. L. Wang, O. Heinonen, et al., Science **349**, 283 (2015).
- [9] S. Woo, K. Litzius, B. Krueger, M.-Y. Im, L. Caretta, K. Richter, M. Mann, A. Krone, R. M. Reeve, M. Weigand, et al., Nat. Mater. **15**, 501 (2016).
- [10] J. Hagemester, E. Y. Vedmedenko, and R. Wiesendanger, Phys. Rev. B **94**, 104434 (2016).
- [11] P.-J. Hsu, A. Kubetzka, A. Finco, N. Romming, K. von Bergmann, and R. Wiesendanger, Nat. Nanotechnol. **Advanced online publication** (2016).
- [12] K. Shibata, J. Iwasaki, N. Kanazawa, S. Aizawa, T. Tanigaki, M. Shirai, T. Nakajima, M. Kubota, M. Kawasaki, H. S. Park, et al., Nat. Nanotechnol. **10**, 589 (2015).
- [13] W. Koshibae and N. Nagaosa, Nat. Commun. **7** (2016).
- [14] B. Dupé, C. N. Kruse, T. Dornheim, and S. Heinze, New J. Phys. **18**, 055015 (2016).
- [15] O. Fruchart, S. Jaren, and J. Rothman, Appl. Surf. Sci. **135**, 218 (1998).
- [16] See Supplemental Material.
- [17] H. Fritzsche, J. Kohlhepp, and U. Gradmann, Phys. Rev. B **51**, 15933 (1995).
- [18] R. Damon and J. Eshbach, J. Phys. Chem. Sol. **19**, 308 (1961).
- [19] L. Baselgia, M. Warden, F. Waldner, S. L. Hutton, J. E. Drumheller, Y. Q. He, P. E. Wigen, and M. Maryško, Phys. Rev. B **38**, 2237 (1988).
- [20] R. Sellmann, H. Fritzsche, H. Maletta, V. Leiner, and R. Siebrecht, Phys. Rev. B **64**, 054418 (2001).
- [21] K. Zakeri, Y. Zhang, J. Prokop, T.-H. Chuang, N. Sakr, W. X. Tang, and J. Kirschner, Phys. Rev. Lett. **104**, 137203 (2010).
- [22] M. Belmeguenai, J.-P. Adam, Y. Roussigné, S. Eimer, T. Devolder, J.-V. Kim, S. M. Cherif, A. Stashkevich, and A. Thiaville, Phys. Rev. B **91**, 180405 (2015).
- [23] L. Udvardi and L. Szunyogh, Phys. Rev. Lett. **102**, 207204 (2009).
- [24] J. Torrejon, J. Kim, J. Sinha, S. Mitani, M. Hayashi, M. Yamanouchi, and H. Ohno, Nat. Commun. **5** (2014).
- [25] A. N. Bogdanov and U. K. Rößler, Phys. Rev. Lett. **87**, 037203 (2001).
- [26] B. Zimmermann, M. Heide, G. Bihlmayer, and S. Blügel, Phys. Rev. B **90**, 115427 (2014).
- [27] N. Nagaosa and Y. Tokura, Nat. Nanotechnol. **8**, 899 (2013).

* Electronic address: lorenzo.camosi@neel.cnrs.fr

Supplemental Materials

SAMPLE GROWTH

The high nucleation density makes Pulsed Laser Deposition (PLD) an excellent technique for the layer-by-layer growth of epitaxial systems. In our set-up, the laser source is a frequency-doubled Nd:YAG laser ($\lambda = 532$ nm) with a pulse duration of approximately 10 ns, a 3 W maximum average power and 10 Hz frequency.

The layer-by-layer growth is investigated in samples with a thickness gradient (wedge). In-situ Reflection High-Energy Electron Diffraction (RHEED) allows us to confirm the epitaxial relationships between the crystals during the deposition.

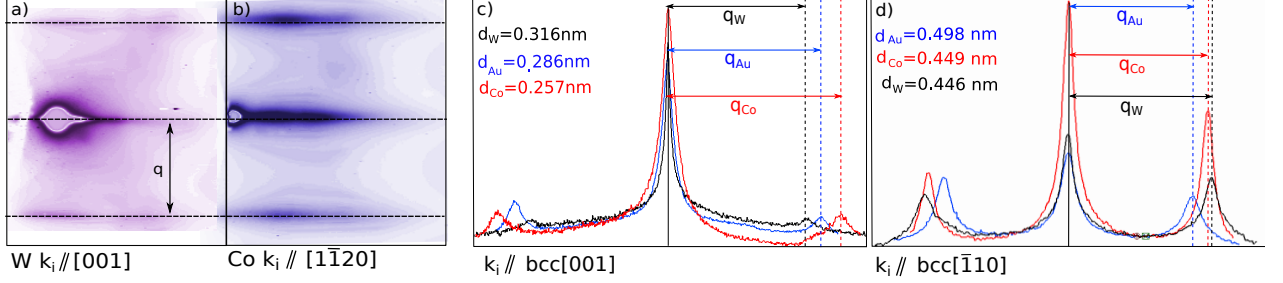


Figure 5: a) RHEED pattern from the W(110) surface with the electron beam parallel to the [001] direction. b) RHEED pattern from the Co surface with the electron beam parallel to the $[1\bar{1}20]$ direction (parallel to the bcc [001] direction). c) d) Plot of the RHEED intensity from the Gold (blue), Cobalt (red) and Tungsten (black) surfaces with the electron beam along the bcc[001] in c) and along the bcc $[\bar{1}10]$ in d)

The Co grows on the bcc W(110) surface following Nishiyama-Wassermann orientation, i.e. with a unique epitaxial relationship and the Co $[1\bar{1}20]$ direction parallel to the W[001] and the Co $[\bar{1}100]$ parallel to the W $[\bar{1}10]$. The RHEED diffraction pattern streaks, (c) in Fig. 5, allow to derive the lattice parameter a in the direction perpendicular to the electron beam:

$$a = \frac{\lambda L}{q} \quad (11)$$

where L is the distance between the detector and the sample and λ is the wave length of the incident beam in the relativistic formulation. The value of a^* , reciprocal of a , can be used to determine the strain of the Co crystal. Fig. 5(c) shows the RHEED pattern for the Co, W and Au surfaces with the electron beam along the bcc[001] direction. We can consider pseudomorphic growth of the Co along this direction on the W substrate even if there is a difference between the Co and W pattern streaks. Indeed the distance between the streaks in the RHEED pattern strongly depends on the geometry of the beam reflection and the geometrical conditions between the two measurements could have slightly changed. This effect can generate an intrinsic error in the position of the pattern streaks. It is possible to evaluate the value of the strain ($\epsilon_{[1\bar{1}0]} = -2.86\%$), which is comparable with the values found for the same system in literature [1–4]. The RHEED pattern with the electron beam along the bcc $[\bar{1}10]$ shows the presence of a relaxed Co structure. Indeed the large misfit between the W and the Co atomic parameters ($a_{W[001]bcc} - a_{Co[001]bcc} = 0.66 \text{ \AA}$) does not allow a pseudomorphic growth. The Co thus grows with a relaxed structure and a fixed atomic distance ratio with respect to the tungsten substrate. In literature, High Resolution Low Energy Electron Diffraction (HR-LEED) was performed on Co/W(110) for different Co thickness reporting a ratio of $\frac{a_{Co}}{a_W} = 3.56/4.56 \frac{a_W}{2} = 0.78$ between 2 and 4 MonoLayers (ML) [17]. Our experimental data show a Co/W atomic distance ratio in agreement with this value ($\frac{a_{Co}}{a_W} = 0.81$). Hence the Co-W crystals produce a superstructure with a twofold symmetry, a period of $14a_y$ ($14a_y - 11a_W/2 = 2 \text{ pm}$) along the W[001] axis and one W atomic distance a_x along the W $[\bar{1}10]$ as shown in Fig. 14.

The system is capped with a thin film of Au. The Co(0001) symmetry allows the epitaxial growth of a fcc(111) Au crystal. It grows in its relaxed configuration due to the big mismatch of the lattice parameters.

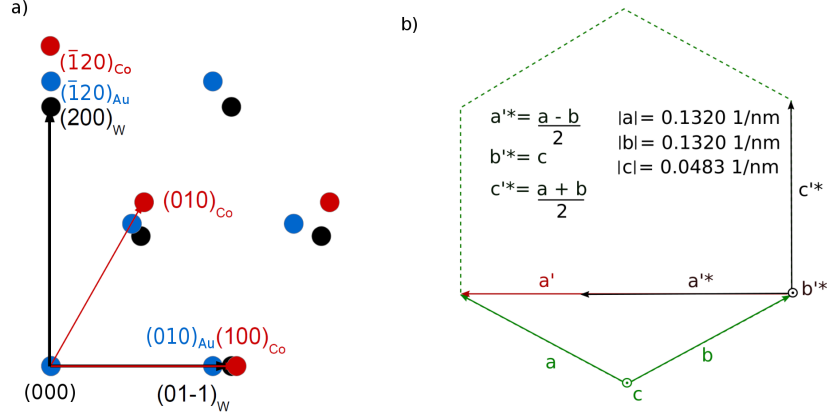


Figure 6: a) Bragg peaks for *fcc* Au(111)/Co(0001)/*bcc* W(110) crystals in their epitaxial relationship b) Sketch of the reciprocal frameworks fixed on the Al_2O_3 crystal used to describe the Bragg peaks and values of the lattice parameter for a Al_2O_3 crystal.

Grazing incidence X-ray diffraction measurements were performed at the BM32 beamline of the European Synchrotron Radiation Facility, on the capped Au/Co/W(110) multilayer with a homogeneous Co layer of 3 ML thickness.

It is possible to describe the Bragg peaks in a reciprocal framework fixed on the Al_2O_3 crystal. The Al_2O_3 crystal has a 3C symmetry whereas the Au/Co/W(110) has a 2C symmetry. Then in order to better describe the W, Co and Au peaks we define a new framework with perpendicular axes as shown in Fig. 6. Hence we can formulate an expression for the points in the reciprocal space:

$$\mathbf{Q} = (Ha'^*, Kb'^*, Lc'^*) \quad |\mathbf{Q}| = \sqrt{(H\sqrt{3}|a|)^2 + (K|c|)^2 + (L|a|)^2} \quad (12)$$

with the reciprocal lattice parameter defined in the Fig. 6. The momentum transfer modulus was scanned in the surface plane ($Q_z = 0.08 \text{ \AA}^{-1}$) along both the *bcc*(001) and *bcc*($\bar{1}10$) directions. In the former case, shown in Fig. 7, three Bragg peaks are observed corresponding to W(002), Au($\bar{1}20$) and Co($\bar{1}20$) reflections, respectively. The registry position of the cobalt layer along the *bcc*($\bar{1}10$) direction is confirmed by the scan of Fig. 8. In this case only one additional peak is observed, attributed to the relaxed Au layer. The Co(100) peak merges with the W($\bar{1}10$) one. Angular scans show that the main crystallographic axes of the cobalt film are aligned with the tungsten ones. Defining β as the angle between the Co bonds 01 and 01' (Fig. 14) it is possible to determine the distortion of the Co crystal. This angle can be calculated from the position of the Co (100) and (010) peaks ($\beta = 0.51$). We can conclude that the Co/W interface is hardly modified by the capping layer.

We also prepared a Co/W(110) sample with a thickness gradient of the Co layer. The layer thickness is calculated a priori using an in-situ quartz crystal microbalance placed before the deposition at the sample position. Fig.(9) shows the STM pictures taken along a Co wedge. The Co islands, as shown in Fig. 9(f), have the height of the Co interplanar distance (2 \AA) and their lateral size increases for increasing values of the Co thickness. The growth is not perfectly layer-by-layer, since in Fig. 9(b) it is possible to detect three atomic levels. However the sample can be considered to have a homogeneous thickness from the magnetic point of view because the characteristic exchange length (l_{ex}) is comparable with the average distance between the islands [5]. These images allow us to have an extra confirmation of the sample thickness. Indeed it is possible to calculate the ratio of surface covered by islands as a function of the position in the wedge. The data, as in Fig. 9(e), are fitted with a Gaussian function for each atomic step. The thickness in ML ($t = n + CR$) is calculated via the islands coverage ratio $CR = \frac{I(n+1)}{I(n+1)+I(n)}$, where $I(n)$ is the Gaussian integral for a given n layer. The higher step linewidth function is fixed using the value of the lower step function. This allows to avoid the apparent broadening of island size due to the STM tip shadow effect.

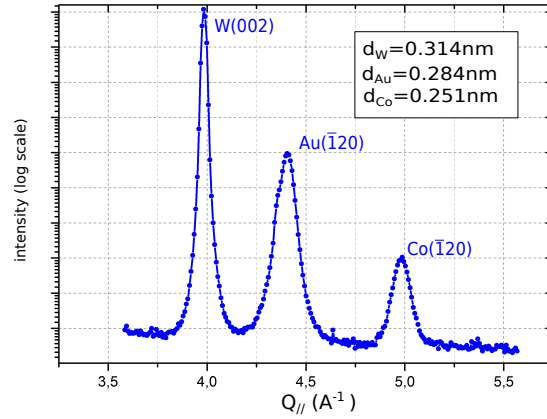


Figure 7: GIXRD measurements performed scanning the momentum transfer parallel to the surface plane, along the $bcc(001)$ direction

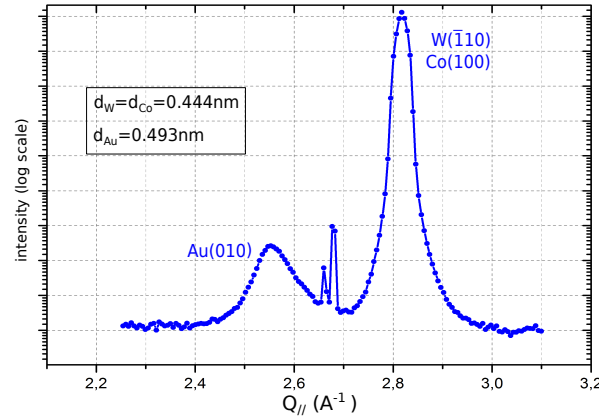


Figure 8: Scan parallel to the $bcc(\bar{1}10)$ direction

OUT-OF-PLANE MAGNETIZATION

We used focussed Kerr magnetometry to study the magnetization reorientation in the sample with a Co wedge. The polar Kerr cycles are measured as a function of an out-of plane magnetic field. The hysteresis loops obtained for different Co thickness are plotted in Fig. 10. For small thickness the Curie temperature is below room temperature, i.e. the correlation between the Co atoms is weaker than the thermal fluctuations. In this regime the Co is paramagnetic and there is no Kerr signal [6]. The black loop in Fig. 10 (1.7 ML) shows the presence of a finite magnetization, a saturation field of $\mu_0 H_{\text{sat}} = 10$ mT and the absence of coercivity. This indicates a superparamagnetic state where the Co islands are ferromagnetic with a weak mutual interaction. The out-of-plane interfacial Magneto-Crystalline Anisotropy is the dominating effect for the thickness range between 1.7 ML and 4.5 ML. Indeed the square hysteresis loop (red line in Fig. 10) for out-of-plane magnetic field shows the presence of an out-of-plane easy axis. The change of shape and the increase of saturation field in the hysteresis when increasing the thickness to 4.8 ML (blue line in Fig. 10) show that the easy axis is not parallel to the applied field any longer. Indeed, when the thickness increases [4.5 – 5.1 ML] the magnetic volume increases and the shape anisotropy progressively tilts the magnetization in the sample plane. The spin reorientation range depends on the strength of the MCA and hence on the surface quality. The spin reorientation transition range is perfectly comparable with the values found by [20]. The complexity of the reflection mechanism in a multi-layer magnetic system does not allow to estimate from the Kerr magnetometry the value of the spontaneous magnetization (M_s). The spontaneous magnetization ($M_s = 1.15 \times 10^6$ A/m) is obtained from the out-of-plane hysteresis loop taken using a Vibrating Sample Magnetometer and the estimation of the magnetic

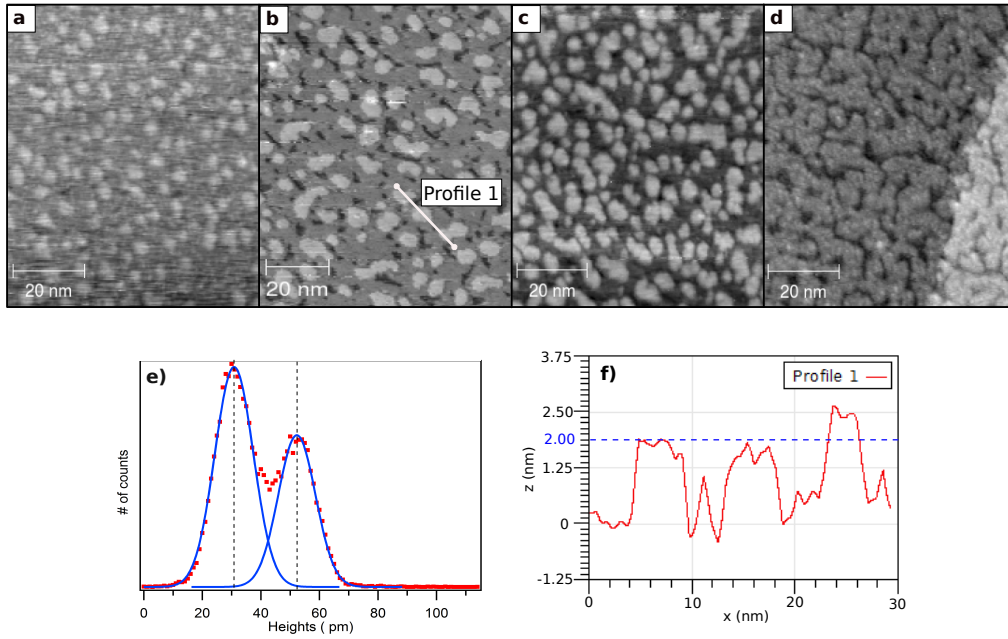


Figure 9: STM pictures of Co islands during a quasi-layer-by-layer deposition in different positions along a Co wedge. a) 1.15 ML b) 1.45 ML c) 1.62 ML d) 1.93 ML are the thickness of the Co layer that can be calculated studying the coverage ratio of Co islands. e) Plot of the heights of the islands as a function of the STM picture (b). f) plot of the islands height along the profile 1 in the STM picture (b)

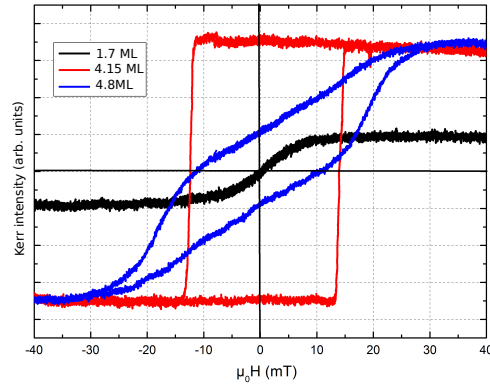


Figure 10: Hysteresis loops obtained by polar focused Kerr on different positions along a Co wedge in Au/Co/W(110).

volume.

PHENOMENOLOGICAL INTERPRETATION OF ANISOTROPIC DMI

The presence of anisotropic DMI in magnetic systems with C2 surface symmetry can phenomenologically be understood considering the Fert-Levy three atoms model [7]. This model considers a magnetic metal crystal and analyzes the indirect magnetic exchange between two magnetic atoms when the conduction electrons scatter with a high spin orbit coupling impurity. The indirect exchange interaction between two magnetic atoms via one electron in the conduction band is described by the RKKY model [8]. In systems with inversion symmetry this interaction is symmetric, promotes collinear spin arrangement and its effect is hidden in the direct Heisenberg exchange. If we consider a sys-

tem with lack of inversion symmetry and spin orbit coupling the symmetry nature of the indirect exchange strongly changes. Indeed the spin orbit coupling sets a relation between the space and spin degrees of freedom and in systems with lack of inversion symmetry a breaking of the exchange symmetry can thus be expected. In the Fert-Levy model the inversion symmetry is broken by the presence of a scattering point not collinear with the magnetic ions. The spin orbit coupling plays its role in the scattering process between the conduction electron and the impurity. The resulting exchange interaction thus will have a symmetric and an antisymmetric component. The antisymmetric one is the DMI-like interaction which promotes a perpendicular spin arrangement. Its Hamiltonian can be formulated [7] :

$$\begin{aligned} H_{DM} &= -V_1 \frac{\sin[\mathbf{k}_f(\mathbf{R}_1 + \mathbf{R}_2 + \mathbf{R}_{12}) + (\pi/10)Z]\hat{\mathbf{R}}_1 \cdot \hat{\mathbf{R}}_2}{\mathbf{R}_1 \mathbf{R}_2 \mathbf{R}_{12}} (\hat{\mathbf{R}}_1 \times \hat{\mathbf{R}}_2) \cdot (\mathbf{S}_1 \times \mathbf{S}_2) \\ &= \mathbf{d}(\mathbf{R}_1, \mathbf{R}_2, \mathbf{R}_{12}) \cdot (\mathbf{S}_1 \times \mathbf{S}_2) \end{aligned} \quad (13)$$

where V_1 is the perturbation potential for the conduction electron gas that depends on the exchange matrix elements between a conduction electron and the d-orbital electrons in the magnetic atoms; in a framework set on the scattering center, \mathbf{R}_1 and \mathbf{R}_2 are the positions of the two magnetic atoms and \mathbf{R}_{12} is the vector between the magnetic ions; the term $(\pi/10)Z$ is the Fermi level phase shift induced by the interaction of the conduction electron with the Z electrons in the d orbital of the scattering point and \mathbf{k}_f is the wavevector of the conduction electron.

The strength and the sign of the interaction strongly depend on the geometry of the triangle composed by the ions and the scattering point. Indeed the DMI vector ($\mathbf{d}(\mathbf{R}_1, \mathbf{R}_2, \mathbf{R}_{12})$) has its direction always parallel to the normal of the triangle and its sign depends on the triangle geometry. In order to understand this dependence we analyze two different cases. All the considerations will be extended to a two dimensional crystal where the \mathbf{d} out-of-plane components are averaged to zero. Hence all the analysis will be developed in a 1D approximation.

- We study the DMI sign and strength fixing the distance between the line connecting the magnetic atoms and the scattering point, which is kept centered in between the magnetic atoms (Fig. 11). The DMI strength in Fig. 11 is thus plotted as a function of the atomic distance R_{12} .

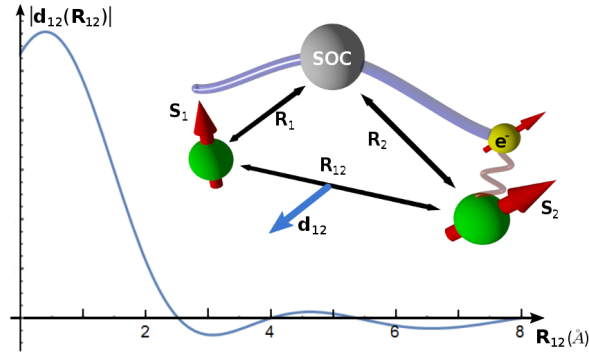


Figure 11: Plot of Eq.(13) as a function of the distance between the magnetic atoms \mathbf{R}_{12} in \AA . The y axis is normalized with respect to the constant V_1 . An artistic picture shows the configuration and the particles that play a role in the three atoms model for the DMI.

- We fix the position of the magnetic atoms and change the scattering point position in a line parallel to the line connecting the magnetic atoms. The DMI strength in Fig. 12 is thus plotted as a function of the distance r .

In both the analyzed cases \mathbf{k}_f is estimated from angle-resolved photoemission spectroscopy measurements performed by Moras et al. [9] on a Co/W(110) interface. The plots in Fig. 11 and 12 evidence the strong dependence of the DMI strength on the geometrical configuration. Indeed a change of the distance between the magnetic atoms and of the scattering point position drastically change the interaction strength and can modify the DMI sign.

We consider the interface between a magnetic crystal and a heavy metal. In this stack the DMI arises from the interface with the high spin orbit coupling metal that breaks the inversion symmetry. The Fert-Levy model can not be

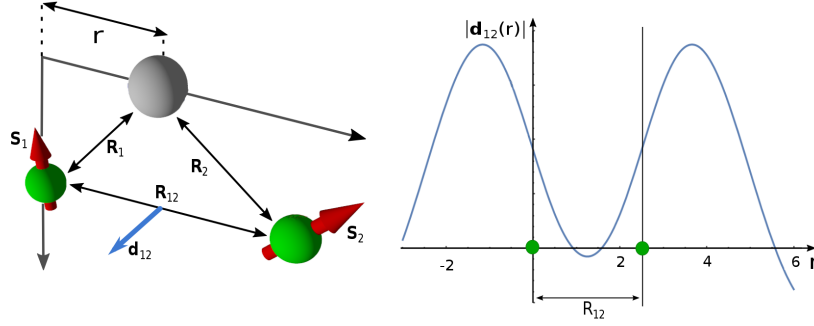


Figure 12: Plot of Eq. (13) as a function of the position of the scattering point \mathbf{r} . The y axis is normalized with respect to the constant V_1 . The distance between the magnetic ions is set equal to 3\AA .

used to have a quantitative interpretation of DMI strength and sign because the interaction can not be reduced to a simple scattering phenomenon. On the other hand we can use this model as a phenomenological tool for determining the crystal symmetry class where it is possible to expect an anisotropic DMI. Indeed we can consider the relationship between the two dimensional unit cells at the interface and take into account one by one the interactions between the magnetic ions with their closer scattering point independently one from the other.

We focus on the magnetic crystal and we consider the scattering points in the center of the bonds. In this approximation we can notice that a C2 crystal allows an anisotropic interaction. Indeed in a rectangular crystal the difference in distance between the two crystallographic directions could induce different strength and sign of the DMI vector. The same argument is not valid for higher symmetry classes like C3 or C4. In these crystals an anisotropic DMI can only be obtained if the scattering points are placed in a different way with respect to the bonds between magnetic atoms.

FROM ATOMIC STRUCTURE TO MICROMAGNETIC DMI IN TWOFOLD SYSTEMS

The micromagnetic DMI is an averaged consequence of the atomic interactions. Hence in order to evidence the relationship between the crystal symmetry and the micromagnetic DMI it is fundamental to analyze the atomic configuration and symmetry of the interface between the magnetic and the heavy metal crystal. This analysis does not aim at the quantitative evaluation of DMI, but to illustrate how atomic DMI vectors \mathbf{d}_{ij} between atoms i and j at various atomic sites add up to yield global micromagnetic D constants along the main symmetry axes of the system.

$$E_{DM} = \sum_{ij} \mathbf{d}_{ij} \cdot (\mathbf{m}_i \times \mathbf{m}_j) \quad (14)$$

Twofold symmetry systems present a particular interest since they can exhibit anisotropic antisymmetric exchange interactions. We will develop the calculations for the Co crystal epitaxially grown on bcc W(110). A schematic view of the Co crystal in its epitaxial relationship with the W substrate is shown in Fig. 13. The big mismatch between the lattice parameters produces the relaxation of the Co crystal along the $\text{bcc}[001]$ direction. In order to consider the full interface symmetry it is important to take into account the produced supercrystal described in Fig. 14, i.e the Co between 2ML and 10ML grows pseudomorphically along the $\text{bcc}[\bar{1}10]$ direction ($a_x = \sqrt{2}/2a_W = 0.223 \text{ nm}$) whereas along the $\text{bcc}[001]$ it grows with a defined proportion with respect to the W ($a_y = 3.56/4.56a_W/2 = 0.124 \text{ nm}$) [see [17]]. It is possible to define a reconstruction period of $14a_x$ where the Co crystal finds the initial relationship with the W ($14a_x - 11a_W = 2pm$).

The Moriya symmetry rules allow to define the direction of each \mathbf{d}_{ij} vector for each ij Co bond. Indeed \mathbf{d}_{ij} is always parallel to the normal of the triangle delimited by the magnetic atoms and the scattering center. By looking at the supercrystal structure displayed in Fig. 14 we can notice how the W atoms drastically change their position with respect to the same Co bond in different unit cells. Thus we can expect \mathbf{d}_{ij} vectors with different strengths and directions. If the analyzed magnetic configurations have a characteristic length (l) much larger than the supercell

parameter ($14a_x$) one can reduce the calculation to a single Co cell with $\langle \mathbf{d}_{ij} \rangle$ vectors as the average of all the \mathbf{d}_{ij} for the same bonds on the superlattice. Along the 03 bond the W atoms are aligned with the Co atoms and the $\langle \mathbf{d}_{03} \rangle$ vectors will lie in the crystal plane. The bonds 01' and 01 are symmetric with respect to the W atoms and they have the same length $|\mathbf{r}_{01}| = |\mathbf{r}_{01'}|$. Then we can expect that the in-plane components will average to zero and consider the vectors having the same modulus ($\langle d \rangle = \langle d_{01'} \rangle = \langle d_{01} \rangle$).

Because of all these considerations we study only one Co cell where we take into account only the interaction between the first neighbors, labeled by 1, 1' and 3 in Fig. 13, and restrict the calculation to $-\frac{\pi}{2} < \alpha < \frac{\pi}{2}$.

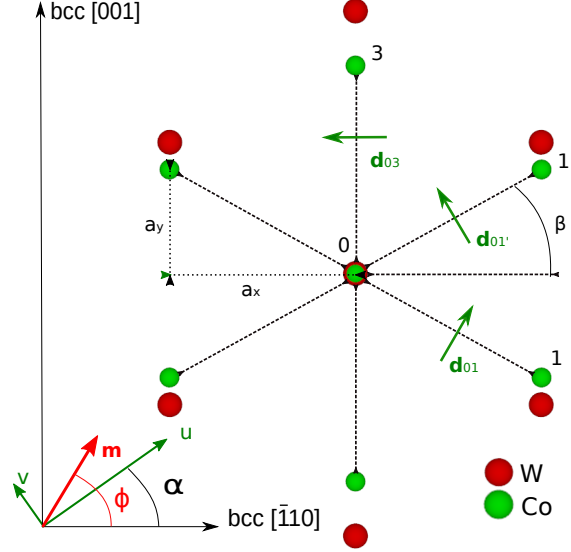


Figure 13: Superposition of the W(110) and the strained Co (0001) surfaces with the Nishiyama-Wassermann relationship with an illustration of notation used to describe the magnetization ($\theta; \phi$) and the directions (α) in the $bcc(110)$ crystal framework

Then in the crystal framework ($\hat{x} // bcc[\bar{1}10], \hat{y} // bcc[001]$) the $\langle \mathbf{d}_{ij} \rangle$ vectors for each bond described by the vector \mathbf{u}_{ij} are:

$$\langle \mathbf{d}_{01} \rangle = -\frac{\langle d_{01} \rangle}{a} [a_y \hat{\mathbf{x}} + a_x \hat{\mathbf{x}}] \quad \langle \mathbf{d}_{01'} \rangle = -\frac{\langle d_{01'} \rangle}{a} [-a_y \hat{\mathbf{x}} + a_x \hat{\mathbf{y}}] \quad \langle \mathbf{d}_{03} \rangle = -\langle d_y \rangle \hat{\mathbf{y}} \quad (15)$$

$$\mathbf{u}_{01} = \frac{a_x \hat{\mathbf{x}} - a_y \hat{\mathbf{y}}}{a} \quad \mathbf{u}_{01'} = \frac{a_x \hat{\mathbf{x}} + a_y \hat{\mathbf{y}}}{a} \quad \mathbf{u}_{03} = \hat{\mathbf{y}} \quad (16)$$

where a is the length of the bond 01' and a_x and a_y the respective projections along the main crystallographic axes (Fig. 14). The case of a large length magnetic configuration, already imposed in the model, allows to describe the magnetization in a continuous medium approach and to express \mathbf{m}_j as the Taylor expansion centered in i

$$\mathbf{m}_j = \mathbf{m}_i + \sum_k |\mathbf{a}_{ij}| \cdot u_{ij}^{(k)} \frac{\partial \mathbf{m}_i}{\partial k} \quad (17)$$

Hence the Eq.(14) takes the form

$$E_{DM} = \sum_i \langle \mathbf{d}_{01} \rangle \cdot [\mathbf{m} \times (a_x \partial_x \mathbf{m} - a_y \partial_y \mathbf{m})] + \langle \mathbf{d}_{01'} \rangle \cdot [\mathbf{m} \times (a_x \partial_x \mathbf{m} + a_y \partial_y \mathbf{m})] + \langle \mathbf{d}_{03} \rangle \cdot [\mathbf{m} \times (2a_y \partial_y \mathbf{m})] \quad (18)$$

$$= \sum_i a_x (\langle d_{01} \rangle + \langle d_{01'} \rangle) \cdot (\mathbf{m} \times \partial_x \mathbf{m}) - a_y (\langle d_{01} \rangle - \langle d_{01'} \rangle - 2\langle d_{03} \rangle) \cdot (\mathbf{m} \times \partial_y \mathbf{m}) \quad (19)$$

$$= - \sum_i 2a_x \frac{\langle d \rangle a_x}{a} \hat{\mathbf{y}} \cdot (\mathbf{m} \times \partial_x \mathbf{m}) - 2a_y \left(\frac{\langle d \rangle a_y}{a} + \langle d_y \rangle \right) \hat{\mathbf{x}} \cdot (\mathbf{m} \times \partial_y \mathbf{m}) \quad (20)$$

Then developing the vectorial and scalar products and using the formalism of the Lifshitz invariants $L_{jk}^{(i)} = m_j \frac{\partial m_k}{\partial i} - m_k \frac{\partial m_j}{\partial i}$ the DM energy can be written

$$E_{DM} = 2 \sum_i \left[a_x \frac{\langle d \rangle a_y}{a} L_{xz}^{(x)} + a_y \left(\frac{\langle d \rangle a_y}{a} + \langle d_y \rangle \right) L_{yz}^{(y)} \right] \quad (21)$$

Hence it is possible to transform the discrete sum in a continuous two-dimensional integral,

$$E_{DM} = 2 \int \left[a_x \frac{\langle d \rangle a_y}{a} L_{xz}^{(x)} + a_y \left(\frac{\langle d \rangle a_y}{a} + \langle d_y \rangle \right) L_{yz}^{(y)} \right] \frac{dx dy}{2a_x a_y} \quad (22)$$

$$= -D_s \int \left[\cot \beta L_{xz}^{(x)} + \left(\frac{\sin \beta + \langle d_y \rangle / \langle d \rangle}{\cos \beta} \right) L_{yz}^{(y)} \right] d^2 r \quad (23)$$

$$= - \int \left[D_s^{(x)}(D_s, \beta) L_{xz}^{(x)} + D_s^{(y)}(D_s, \beta) L_{yz}^{(y)} \right] d^2 r \quad (24)$$

the equation presents a two-fold symmetry with two DMI constants $D_s^{(x)} = D_s \cot \beta$ and $D_s^{(y)} = D_s \frac{\sin \beta + \langle d_y \rangle / \langle d \rangle}{\cos \beta}$ that depend on three parameters $D_s = \frac{\langle d \rangle}{a}$, $\beta = \arctan(a_y/a_x)$ and $\langle d_y \rangle / \langle d \rangle$. The experimental values of $D_s^{(i)}$ along the main axes allow to estimate the factors D_s and $\langle d_y \rangle / \langle d \rangle$.

SPIN TEXTURE AND EFFECTIVE DMI IN A 2-FOLD SYMMETRY SYSTEM

It is possible to generalize the discussion above to every ultra-thin magnetic film with interfacial DMI and a twofold symmetry. Considering a new basis $(\hat{u}, \hat{v}, \hat{z})$ (see Fig. 13), turned by an angle $\alpha = (\hat{x}, \hat{u})$ with respect to the initial basis, the DMI energy of a one-dimensional spin modulation propagating along \hat{u} reads:

$$E_{DM}(\alpha) = - \int \left[\cos^2(\alpha) D_s^{(x)} + \sin^2(\alpha) D_s^{(y)} \right] L_{uz}^{(u)} d^2 r - \int \left(D_s^{(x)} - D_s^{(y)} \right) \cos(\alpha) \sin(\alpha) L_{uz}^{(v)} d^2 r. \quad (25)$$

It presents two different types of Lifshitz invariants that describe a DMI stabilizing different spin configurations in competition. It means that in a general two-fold system the DMI promotes Néel cycloids along the main axes and a mixed configuration between a Néel cycloid and a Bloch spiral along the intermediate directions.

In order to understand the BLS data at $\alpha = \pi/4$, we evaluate the DMI energy for a SW described as $\mathbf{m}(u) = \mathbf{M} + \delta \mathbf{m}(u)$, with $\mathbf{M} = \sqrt{1 - \delta m^2} \hat{v}$ (parallel to \mathbf{H}_{ext} , due to the DE geometry) and $\delta \mathbf{m}(u) = \delta m [\sin(k_{sw} u - \omega t) \hat{u} + \cos(k_{sw} u - \omega t) \hat{z}]$ lying in the (\hat{u}, \hat{z}) plane. The latter expresses the spin-wave of wave vector k_{sw} . Averaging over one wave length $\Lambda = 2\pi/k_{sw}$, the DMI energy density ω_{DM}^{sw} of the texture is

$$\omega_{DM}^{sw} = \frac{2\pi}{\Lambda} \left[\cos^2(\alpha) D_s^{(x)} + \sin^2(\alpha) D_s^{(y)} \right] \delta m. \quad (26)$$

The $2\pi/\Lambda$ factor arises from the fact that over one period, the varying part of the magnetization undergoes a 2π rotation and the δm factor increases the amplitude of the spin-wave. As the spin-wave has a Néel structure, only

the energy part associated to $L_{uz}^{(u)}$ remains. Therefore, an apparent DMI constant $D_s^{(app)}$ is estimated as $D_s^{(app)} = \omega_{DM}^{sw} \Lambda / 2\pi \delta m$. As a function of α , we find

$$D_s^{(app)} = D_s^{(x)} \cos^2 \alpha + D_s^{(y)} \sin^2 \alpha \quad (27)$$

The plot of Eq.(27) in Fig. 14(b) shows a very good agreement with the experimental data.

In a more general case, the rotation plane of a spin spiral is free in order to minimize the energy. Writing ϕ as the angle of such a plane with respect to the \hat{x} axis (Fig. 13), we estimate, using a similar calculation as for the spin-wave, the optimum relation between ϕ and α :

$$\tan \phi = \left(\frac{D_s^{(y)}}{D_s^{(x)}} \right) \tan \alpha \quad (28)$$

with an effective DMI constant

$$D_s^{eff} = D_s^{(x)} \cos \alpha \cos \left[\arctan \left(\frac{D_s^{(y)}}{D_s^{(x)}} \tan \alpha \right) \right] + D_s^{(y)} \sin \alpha \sin \left[\arctan \left(\frac{D_s^{(y)}}{D_s^{(x)}} \tan \alpha \right) \right] \quad (29)$$

* Electronic address: lorenzo.camosi@neel.cnrs.fr

† Electronic address: jan.vogel@neel.cnrs.fr

- [1] R. Sellmann, H. Fritzsche, H. Maletta, V. Leiner, and R. Siebrecht, Phys. Rev. B **64**, 054418 (2001).
- [2] H. Fritzsche, J. Kohlhepp, and U. Gradmann, Phys. Rev. B **51**, 15933 (1995).
- [3] M. Pratzer, H. Elmers, and M. Getzlaff, Phys. Rev. B **67**, 153405 (2003).
- [4] J. H. Van der Merwe, D. L. Tonsing, P. M. Stoop, and E. Bauer, Phys. Rev. B **49**, 2127 (1994).
- [5] S. Andrieu, C. Chatelain, M. Lemine, B. Berche, and P. Bauer, Phys. Rev. Lett. **86**, 3883 (2001).
- [6] G. Garreau, M. Farle, E. Beaurepaire, and K. Baberschke, Phys. Rev. B **55**, 330 (1997).
- [7] A. Fert and P. M. Levy, Phys. Rev. Lett. **44**, 1538 (1980).
- [8] M. A. Ruderman and C. Kittel, Phys. Rev. **96**, 99 (1954).
- [9] P. Moras, G. Bihlmayer, P. Sheverdyaeva, S. Mahatha, M. Papagno, J. Sánchez-Barriga, O. Rader, L. Novinec, S. Gardonio, and C. Carbone, Physical Review B **91**, 195410 (2015).

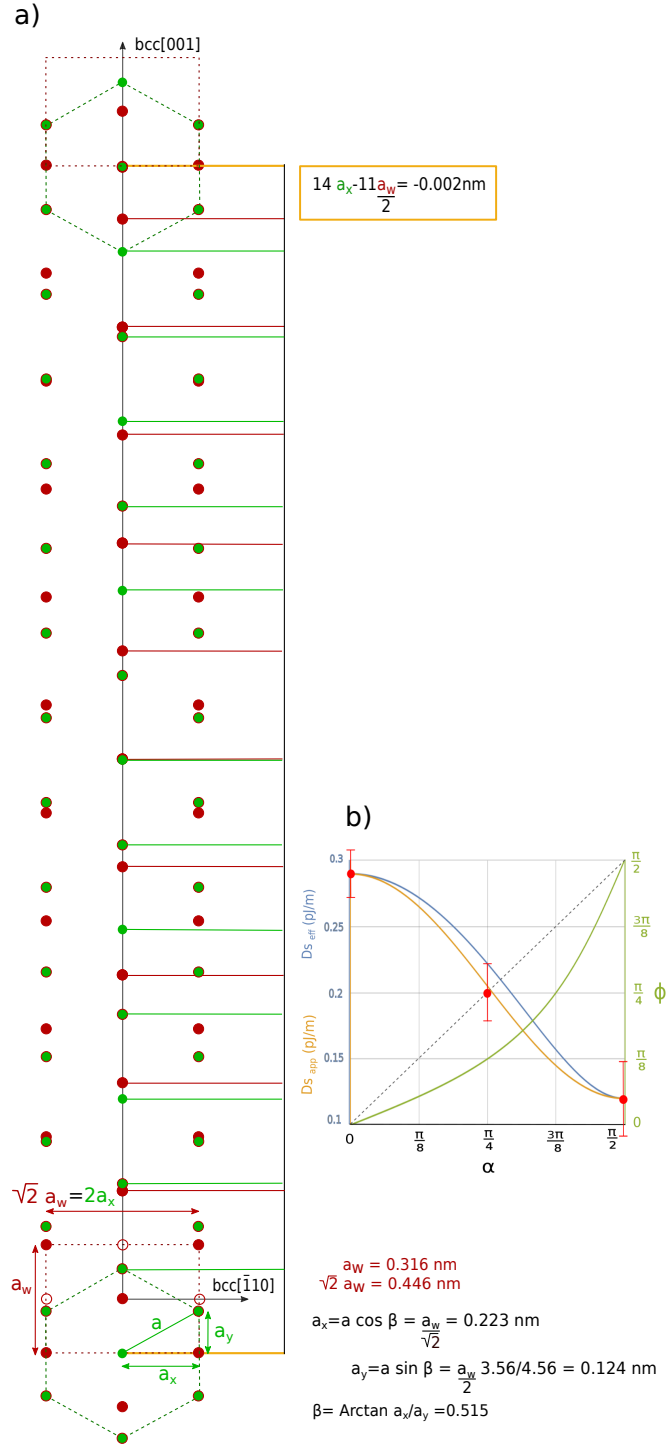


Figure 14: **(a)** Sketch of the supercrystal produced by the epitaxial growth of the Co(0001) surface on the bcc W(110) surface. **(b)** Blue and orange lines : micromagnetic calculated $D_s^{(\text{eff})}$ (Eq.29) and $D_s^{(\text{app})}$ (Eq.27) as a function of the in-plane directions (ϕ); red dots: D strength evaluated from the experimental data; green line: micromagnetic calculated magnetization promoted by DMI (Eq.28) as a function of the crystallography directions; dashed line: Néel-like cycloid